ASME Journal of Tribology
Online journal at:
https://asmedigitalcollection.asme.org/tribology

High-Speed Recessed Conical Hybrid Bearings With Additive Manufacturing–Driven Large Gap Clearances for Integrated Bearing–Rotor Architectures of Gas Turbines: Navier–Stokes Analysis and Symbolic–Regression Correlations

Ahmet Yıldırım
Department of Mechanical Engineering,
İzmir Katip çelebi University,
İzmir 35620, Turkey
e-mail: ahmetyildirim1996@gmail.com

Sercan Acarer
Department of Mechanical Engineering,
İzmir Katip çelebi University,
İzmir 35620, Turkey
e-mail: sercan.acarer@ikcu.edu.tr

Beni Cukurel[1]
Department of Aerospace Engineering,
Technion—Israel Institute of Technology,
Haifa 32000, Israel
e-mail: beni@cukurel.org

Hydrostatic recessed conical bearings operating at high rotational speeds, commonly referred to as hybrid bearings, exhibit several advantages, including structural simplicity, reduced maintenance requirements, superior high-speed performance, increased load-carrying capacity, and lower noise and vibration. Existing hybrid-bearing research has so far primarily focused on small clearances, cavitation-free operation, and peripheral speeds up to roughly 90 m/s. However, advances in additive manufacturing now permit integrated, optimized bearing–rotor architectures, where clearances of 300 μm and turbomachinery-level peripheral speeds above 200 m/s are unavoidable. Under these conditions, the presence of recesses on a conical base, combined with three-dimensional flow effects and cavitation phenomena, renders classical hydrodynamic theory and existing design practices inadequate, thereby necessitating the use of new models. To address these challenges, a Design-of-Experiments approach, integrated with Navier–Stokes simulations, was employed to systematically analyze load capacity, frictional losses, and flowrates as a function of bearing geometry, clearance, supply pressure, recess configuration, semi-cone angle, rotational speed, and fluid properties. This study presents models derived via symbolic regression, capturing relationships among nondimensional design parameters of high-speed hybrid bearings with large clearances under additive manufacturing constraints, complemented by design charts and simulation results to support efficient design and analysis. [DOI: 10.1115/1.4070628]

Keywords: hybrid bearings, hydrostatic recessed conical bearings, tribology, symbolic regression, design of experiments., additive manufacturing, bearing design and technology, cavitation, hydrostatic lubrication, pressurized bearings

1 Introduction

The lubrication bearings, with high-speed operation capability and long service life, are central to power and propulsion systems, which feature high-speed turbomachinery [1]. In hydrostatic bearings, an external pump delivers pressurized lubricant to the bearing clearance, establishing a continuous fluid film that physically separates the stationary and rotating elements, thereby eliminating metal-to-metal contact and significantly reducing wear. Hydrodynamic bearings, by contrast, generate the supporting pressure by the relative rotation of the shaft, which drags the viscous lubricant into a converging wedge-shaped gap, where shear-induced momentum transport produces a load-carrying pressure distribution. Hybrid bearings combine these two mechanisms, using externally supplied pressure in addition to self-generated hydrodynamic support at high rotational speeds.

In hydrodynamic bearing design, the Reynolds lubrication theory provides the principal analytical framework. Widely adopted design guidelines have been developed based on this

---

[1] Corresponding author.

Contributed by the Tribology Division of ASME for publication in the Journal of Tribology. Manuscript received October 4, 2025; final manuscript received December 1, 2025; published online January 27, 2026. Assoc. Editor: Jean Bouyer.

theory and validated through measurements [2–4]. More recently, machine learning algorithms have also been employed in predictive analysis, utilizing numerically generated datasets based on the Reynolds equation to assess performance metrics such as maximum pressure, minimum film thickness, Sommerfeld number, load, and rotational speed, with results shown under steady-state hydrodynamic lubrication conditions [5]. Similarly, experimental data were used to train artificial neural networks to predict the friction coefficient and bearing temperature as a function of radial load and rotational speed under conditions of small clearances, demonstrating the reliability and accuracy of neural network models for such applications [6].

For externally pressurised (hydrostatic) journal bearings, the dimensionless performance parameter $S_h = \frac{\eta N}{P_s (c_d/D)^2}$ is often used to guide the design towards minimizing power loss and leakage while maximizing stiffness [7]. By including diametral clearance (c_d), bearing journal diameter (D), lubricant viscosity (η), supply total pressure (P_s) and journal angular speed (N), recommended values of this parameter result in minimal hydrodynamic action and prevent cavitation. More detailed studies also consider additional key design parameters, such as the length-to-diameter ratio, eccentricity ratio, shaft speed, recess-to-bearing area ratio, and the number of recesses [8,9].

While hydrostatic and hydrodynamic bearings each offer distinct advantages, hybrid bearings combine the principles of both systems to enhance load-carrying capacity and stability, particularly at high rotational speeds. It has been shown that hybrid journal bearings can achieve higher load support and lower power dissipation. In this regard, guidelines for small clearances are provided to maximize load capacity while minimizing total power dissipation [10]. The high-speed test facility at Texas A&M University evaluated a water-lubricated hybrid journal bearing at up to 2.5×10^4 rev/min, corresponding to a maximum peripheral speed of approximately 100 m/s. Measured bearing displacement, transmitted torque, recess pressure, lubricant flowrate, and bulk temperature exhibited excellent agreement with Reynolds-averaged Navier–Stokes (RANS) simulations; the discrepancy in load-carrying capacity remained below 5.79 % across all test conditions [11].

The aforementioned studies were for journal (cylindrical) bearings. Conical bearings, which have the capability to support combined radial and axial loads, require separate analysis. In this regard, Nypan et al. [12] derived design curves based on the first principles that minimize friction across both laminar and turbulent flow regimes for externally pressurized conical bearings without hydrodynamic effects. Finite element modeling has also been applied for greater predictive fidelity. Using this approach without hydrodynamic coupling, Sharma et al. [13] showed that a larger semi-cone angle raises axial load capacity while lowering lubricant throughput. In a similar study, but with hydrodynamic effects included [14], it was found that increasing the semi-cone angle lowers the required supply total pressure for radial load support while enhancing axial load capacity.

Rowe [15] presents a comprehensive survey of hybrid conical bearings, encompassing three- and four-recess configurations and their single-cone and opposed-cone variants over both low- and high-speed regimes. The study includes design-aid charts intended for preliminary engineering applications. The analysis is primarily qualitative and focused on small clearance ratios, and it does not provide predictive operating coefficients.

In summary, research and applications of hybrid bearings have thus far concentrated on journal (cylindrical) bearings, small clearances, cavitation-free operation, and maximum peripheral speeds up to approximately 90 m/s (Table 1). Advances in Additive Manufacturing (AM) additionally permit integrated, optimized bearing–rotor architectures, where clearances of 100–300 μm and turbomachinery-level peripheral speeds above 200 m/s are unavoidable, greatly increasing Reynolds numbers and cavitation risk. Toward this potential, Palman et al. [16] assessed a double-cone hybrid bearing fabricated with AM-dictated large clearances of up to 300 μm. Computational Fluid Dynamics (CFD) analyses confirmed stable operation at these enlarged gaps: power losses met design targets, while axial and radial load capacities surpassed specifications. The results point toward AM-integrated hybrid bearings for next-generation compact turbine power systems. Despite these promising findings, the parameter space of AM-integrated hybrid bearings has not been comprehensively explored, and further studies are required to assess alternative designs and performance limits.

The present study undertakes a design-space analysis of additively manufactured conical hybrid bearings operating at elevated Reynolds numbers. A coupled CFD and design-of-experiments

Table 1 Summary of reported nominal clearances, maximum peripheral speeds, and semi-cone angles

Type	Clearance (c) and c/D	Peripheral speed (m/s)	Semi cone angle (deg)	Explanation
Four-pad tilting pad journal bearing	$c = 0.235$ mm ($c/D = 8.4 \times 10^{-4}$)	<58.6	0	Experimental characterization of a large tilting pad journal bearing [1]
Non-recessed hydrodynamic journal bearing	$c = 0.45$ mm ($c/D = 9 \times 10^{-4}$)	<3.4	0	A data-driven prediction method for journal bearing performance [5]
Hydrodynamic plain journal bearing	$c = 0.0125$ mm ($c/D = 3.1 \times 10^{-4}$)	<6.3	0	Predicting the friction coefficient of hydrodynamic journal bearings using an artificial neural network trained on experimental load and speed data [6]
Multi-recess hydrostatic journal bearing	$c = 0.0635$ mm ($c/D = 1 \times 10^{-3}$)	8	0	Design methodology for multi-recess hydrostatic journal bearings for minimum power loss at low speeds [8]
Multi-recess hydrostatic journal bearing	$c = 0.05$ mm ($c/D = 5 \times 10^{-4}$)	~0	0	Analysis of load capacity and oil flow in journal bearings using computer-based Reynolds equation solutions [9]
Orifice compensated five-recess-hybrid bearing	$c = 0.0762–0.1016$ mm ($c/D = 1.3 \times 10^{-3}$)	<90	0	Experimental and theoretical analysis of high-speed hybrid journal bearing [11]
Four-pocket hydrostatic conical journal bearing	Dimensionless fluid film thickness (0.02–0.025)	0	10–40	Theoretical study of four-pocket hydrostatic conical journal bearings using FEM [13]
Conical hydrodynamic journal bearing	$c = 0.05$ mm ($c/D = 1 \times 10^{-3}$)	2.6	5–30	Theoretical performance analysis of conical hydrodynamic journal bearings using FEM for varying semi-cone angles [14]
Present study	$c = 0.1–0.3$ mm ($c/D = 2$ and 6×10^{-3})	212.58	10–30	Compatible with AM-based, integrated bearing–rotor architectures for gas turbines [16].

(DoE) framework, supplemented by symbolic regression (SR), is employed to quantify bearing performance, extract dimensionless scaling laws, and elucidate the trade-off between load-carrying capacity and power dissipation. The resulting correlations provide design guidance for next-generation turbomachinery featuring AM-integrated bearing–rotor assemblies.

2 Manufacturing Feasibility Assessment

The manufacturing feasibility of additively manufactured, integrated bearing–rotor architectures, with emphasis on the engine's hydrostatic bearing, was investigated through a systematic evaluation of additive manufacturing constraints and the derivation of design parameters suited to bearing functionality. High-fidelity simulations were carried out on concentric, pre-assembled cone geometries, manufactured together in a single build, with varying cone angles and nominal surface-normal gaps that were designed to remain non-contacting.

Using Simufact Additive Software, a mathematical model was developed to simulate the powder bed fusion process [17] and predict the manufactured (realized) surface-normal gap dimensions, accounting for both the build stage and post-build removal from the platform. The analysis followed a sequential thermo-mechanical finite element approach, beginning with a transient heat transfer simulation to determine the thermal history of each node, followed by a stress analysis based on the resulting temperature gradients. The model employed a uniform cubic mesh of 0.5 mm for the part and 5 mm for the build plate, with material properties defined as Inconel 718 powder for the component and 316L stainless steel for the substrate. The build process was simulated for an EOS M290 printer (Krailling/Munich, Germany) using spherical Inconel 718 powder (14–63 μm particle size). Process parameters included a laser power of 285 W, scanning speed of 960 mm/s, hatch spacing of 120 μm, and powder layer thickness of 40 μm, corresponding to an energy density of about 62 J/mm^3. A strip scanning strategy with 10-mm stripe width and 67-deg rotation between successive layers was adopted to reduce residual stresses and enhance structural isotropy. These conditions enabled accurate prediction of thermal distortion, residual stress distribution, and clearance deviations, forming the basis for pre-deformation optimization of the rotor-bearing geometry. The analysis compared nominal and predicted surface-normal gaps for cone angles of 45 deg, 67 deg, and 90 deg, over a nominal gap range of 75–300 μm.

Based on the simulation results, it is evident that the cone angle exerts a pronounced influence on the actual (realized) gap dimensions. The lowest dimensional accuracy relative to the nominal gap was observed for pre-assembled cones with a 45-deg angle, whereas the highest accuracy was achieved for those with a 90-deg angle. These findings are consistent with previously reported results in the literature, which underscore the inherent limitations of powder bed fusion processes in the fabrication of overhanging structures, as reviewed in Ref. [16]. The results presented in Fig. 1 demonstrate that pre-assembled cones with angles of 45 deg and 67 deg can be successfully manufactured; however, these geometries exhibit comparatively larger deviations from the nominal gap dimensions.

To validate these findings, several pre-assembled cones were fabricated. A survey of the relevant literature indicates that conventionally manufactured hydrodynamic bearings can operate reliably with minimal journal displacement, accommodating gaps of up to approximately 180 μm [16]. The analysis results (Fig. 1) indicate that, for a 45-deg cone, an actual clearance below 180 μm can be achieved when the nominal gap is set to 225 μm or less. Based on these findings, pre-assembled cones with a 45-deg angle and nominal gap sizes between 225 μm and 175 μm were fabricated. For comparative purposes, a 60-deg cone with a nominal gap size of 150 μm and a 90-deg cone with a nominal gap size of 100 μm were also produced (Fig. 2).

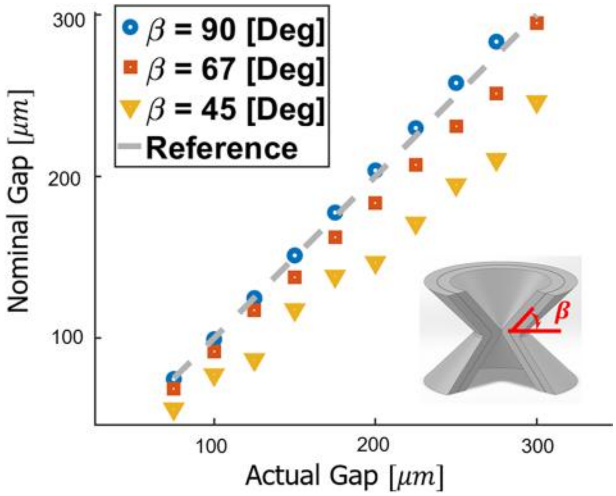

Fig. 1 Nominal to actual surface-normal gap comparison of pre-assembled cones

All printed cones exhibited measurable gaps between the sliding surfaces, confirming a strong correlation with the simulation predictions. All cones displayed rotational freedom in the manufactured specimens. The successful fabrication of these components confirms the manufacturability of the design and enables progression toward evaluating the feasibility of producing an engine rotor within an integrated bearing housing. Nevertheless, due to the rotor's complex geometry, featuring sliding surfaces with substantial overhang angles, achieving a defect-free clearance below 300 μm is considered impractical under the current process parameters. Consequently, a rotor design with a nominal clearance of 300 μm can be considered as feasible.

Optimization of powder bed fusion process parameters offers the potential to mitigate defect formation, enhance the surface quality of overhanging features, and permit greater overhang angles, thereby enabling the fabrication of rotors with clearances below 300 μm. However, it must be acknowledged that process parameters simultaneously affect a wide range of material properties, including yield strength, tensile strength, elongation at break, and pore size distribution. Previous experience in parameter optimization indicates that these properties often exhibit weak or nonlinear correlations. As a result, tailoring process parameters to simultaneously minimize residual stresses and geometric distortions remains a significant technical challenge [16].

3 Methodology

Building on the established printability of pre-assembled concentric cone pairs, a conical hydrostatic bearing with a large nominal clearance was adopted as the fundamental configuration (Fig. 3). The bearing operates by supplying pressurized lubricant into recesses (pockets), generating a thin fluid film on the landing regions. This film separates the shaft from the bearing surface, minimizing friction and wear while enhancing load-carrying capacity. This single-cone bearing features two outlet sections (one in each axial end), four inlet sections inside the evenly distributed pockets (each with a width of 60 deg), and an internal shaft. The axial width (a) determines the recess size, influencing lubricant distribution. The nominal clearance (c) affects the fluid film thickness, while the shaft length (L) and maximum diameter (D) define the overall bearing dimensions.

As a starting point for the preliminary analysis, which involved mesh dependency evaluation and the demonstration of fundamental flow characteristics, a representative geometry was constructed using parameter values recommended in the literature [15,16], including a land-to-pocket ratio of $\frac{a}{L} = 0.25$, a length-to-diameter ratio of $\frac{L}{D} = 0.75$, a semi-cone angle of 20 deg and an eccentricity

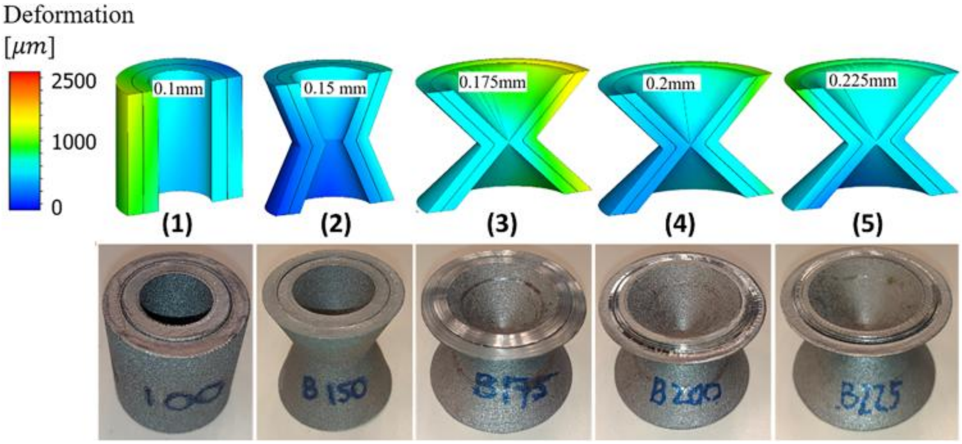

Fig. 2 Rotating test specimens (top) deformation maps, (bottom) printed cones: (1) cone angle: 90 deg, clearance: 100 μm; (2) cone angle: 60 deg, clearance: 150 μm; (3) cone angle 45 deg, clearance: 175 μm; (4) cone angle: 45 deg, clearance: 200 μm; and (5) cone angle: 45 deg, clearance: 225 μm

ratio of 0.5. The eccentricity ratio is defined as the ratio of the distance between the centers of the two cones to the nominal gap between the cones. Other geometric parameters, such as the cone maximum diameter of $D = 90$ mm and the radial clearance of $c = 300\,\mu$m, were determined based on the analysis carried out in Sec. 2. Considering potential micro gas turbine applications, the shaft is envisioned to operate at a rotational speed of 58,000 rpm; the supply total-to-exit static pressure difference is set at 15 bar [19]. Considering the gas turbine architecture envisioned in Ref. [16], the compressor discharge total pressure acts as the bearing exit static pressure. The exit static pressure is therefore taken as 3.7 bar, suitable for gas turbine operation with single-stage centrifugal compressor [16,20].

Steady-state RANS simulations were conducted in Fluent Software [21] using a pressure-based mixture multiphase model. All governing equations were discretized using second-order upwind schemes. Gradients were evaluated with the least-squares cell-based method; pressure was interpolated with the staggered grid approach (Fluent's PRESTO Scheme), and pressure–velocity coupling employed the segregated SIMPLEC algorithm with skewness correction [21]. The SIMPLEC (Semi-Implicit Method for Pressure-Linked Equations–Consistent) scheme is an improved form of the standard SIMPLE algorithm that enhances convergence by modifying the pressure–velocity correction relationship. It reduces the dependency between successive corrections, allowing faster and more stable convergence, especially in flows with strong pressure gradients or complex geometries.

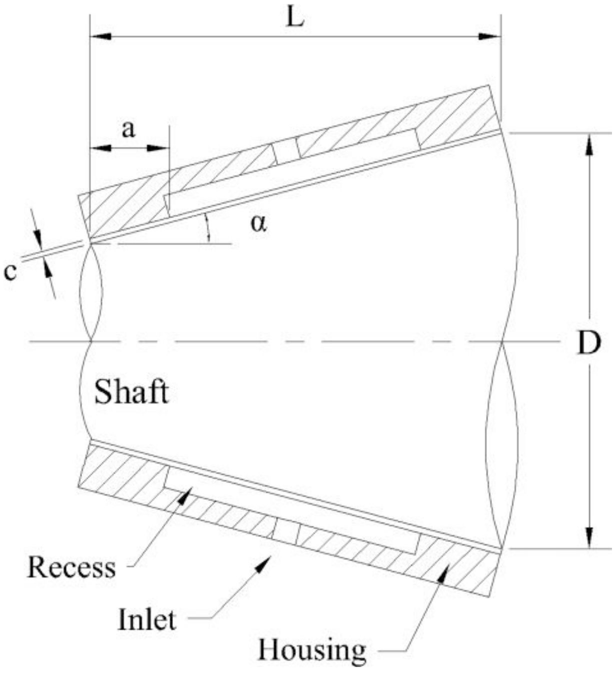

Fig. 3 Layout and parametrization of conical hydrostatic bearing [18]

The realizable k–ε turbulence model with Fluent's enhanced wall treatment [21] is employed to capture near-wall turbulence. Kerosene was used as the operating lubricant. Cavitation within the bearing was modeled using the Zwart–Gerber–Belamri two-phase approach, which represents vapor generation and condensation based on local pressure variations relative to the fluid's vapor pressure. The model assumes a uniform bubble size and applies empirical coefficients to govern the rates of vaporization and condensation, providing a stable and practical framework for simulating cavitation in lubricated flows [21].

The liquid and vapor phases were assigned densities of $780\,\mathrm{kg/m^3}$ and $7.1\,\mathrm{kg/m^3}$, and dynamic viscosities of $2.4 \times 10^{-3}\,\mathrm{Pa \cdot s}$ and $7 \times 10^{-6}\,\mathrm{Pa \cdot s}$, respectively. The vaporization pressure was specified as 700 Pa.

Convergence was declared when all scaled residuals fell below 10^{-5} and integral monitors (bearing load, leakage rate, and peak vapor volume fraction) varied by <0.1% over at least 250 consecutive iterations.

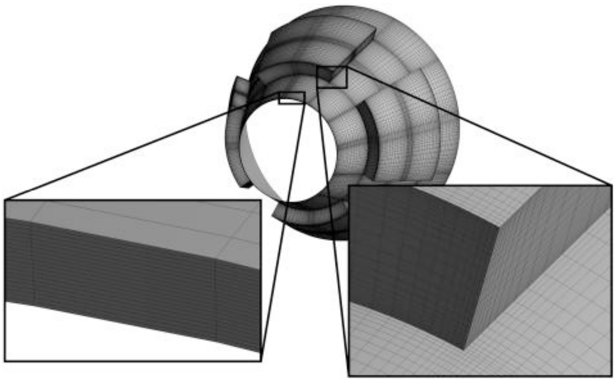

Fig. 4 The hexahedral mesh structure

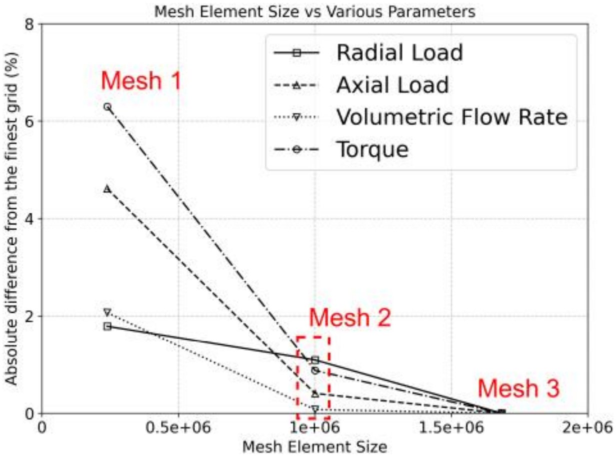

Fig. 5 Mesh sensitivity analysis

3.1 Mesh Independency Study and Validation. The fluid domain was discretized with a structured hexahedral mesh (Fig. 4) with a minimum orthogonal quality of 0.5. A comprehensive mesh sensitivity analysis is undertaken to ascertain the influence of mesh density on the simulation outcomes, varying from 2.4×10^5 elements to the finest at 1.7×10^6 elements. Among these, an intermediate value of 1×10^6 is chosen as a good compromise, which provides a 20-layer discretization of the film thickness and demonstrates a mere 2% discrepancy compared to the finest mesh in radial and axial load, as well as torque and flowrates (Fig. 5).

To ascertain the accuracy of the simulatory framework, a verification study is conducted based on the work presented in Ref. [22]. In their study, CFD simulations were carried out using CFX-TASC flow and were cross-validated against the VT-EXPRESS code [22]. VT-EXPRESS, serving as a reduced-order model, calculates the performance characteristics of hydrostatic and hydrodynamic bearings. The simulations focused on a four-recessed hybrid journal bearing, as shown in Fig. 6. This bearing has 30-mm diameter, 20-mm width, and 0.03-mm clearance. Each pocket of the bearing has distinct features: an included angle of 45 deg, 5-mm axial land width, 1-mm pocket depth, and 0.6mm orifice diameter. Lubricating oil is supplied at a pressure of 5 MPa at each orifice inlet, with a dynamic viscosity of 9.93×10^{-3} Ns/m^2. The rotor operates with an eccentricity ratio of 0.5. After completing CFD simulations on this geometry, a comparative analysis is performed, focusing on inlet pocket pressures, load capacity, and mass flowrates. The results of our simulations matched the results obtained from VT-EXPRESS, within a maximum discrepancy of 2.1% in pocket inlet pressure and less than 0.5% in load capacity (Table 2).

In addition to the model verification, a validation study was also conducted using the experimental results from Kurtin et al. [11]. This study centered on a five-recessed journal bearing, as depicted in Fig. 7. The key geometric parameters are as follows: a diameter and length of 76.2 mm, a radial clearance of 0.0762 mm, and five square recesses measuring 27×27 mm with a uniform depth of 0.254 mm. The simulations were performed at a rotational speed of 1.75×10^4 rpm, using water as the lubricant with a supply pressure of 5516 kPa, and under various eccentricity ratios. As shown in Fig. 8, the numerical results are in good agreement with the experimental data, with a minimum prediction error of 4.8% and a maximum of 9.66%.

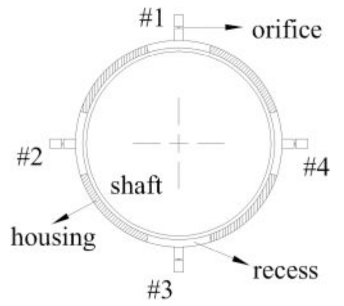

Fig. 6 Schematic representation of the bearing geometry used in a validation study

Table 2 The verification results for the hybrid-bearing test case [22]

	Present CFD study	Reference CFD study	VT Express	% Difference
Pocket 1 Inlet Pressure (MPa)	2.666	2.671	2.724	2.1
Pocket 2 Inlet Pressure (MPa)	3.699	3.723	3.745	1.2
Pocket 3 Inlet Pressure (MPa)	4.982	4.980	4.987	0.1
Pocket 4 Inlet Pressure (MPa)	4.473	4.413	4.503	0.7
Load capacity (N)	674	727	670.9	0.4

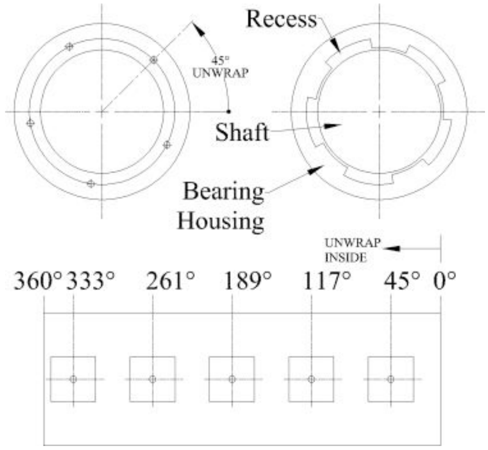

Fig. 7 Hydrostatic bearing test bearing geometry [11]

The results of this validation, in conjunction with the initial verification case, demonstrate good agreement with the numerical

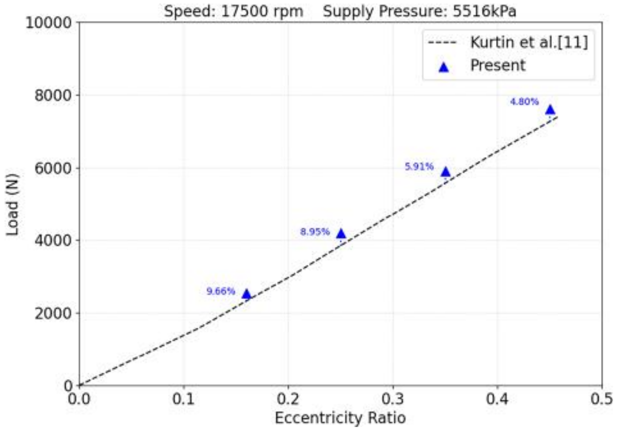

Fig. 8 CFD Model validation against experimental data [11]

predictions, confirming that the present analyses are capable of accurately capturing the underlying physics of hybrid bearings.

3.2 Nondimensionalization of Parameters. The functional relationship defining the fluid dynamics of the conical bearing under the considered constraints is given as:

$$W_r, W_a, F, Q = f(a, L, D, U, c, \rho, \mu, \Delta P, \alpha) \tag{1}$$

In this relationship, a is the bearing land axial width, L is the axial length of the bearing, D is the maximum diameter of the shaft (Fig. 1), U is the tangential speed at the maximum radius, ΔP is the total-to-static pressure difference, μ is the dynamic viscosity, ρ is the density of the lubricant, α is the semi-cone angle, c is the nominal clearance, W_r is the radial load capacity, W_a is the axial load capacity, F is the friction power loss, and Q is the volume flowrate. The Buckingham Pi Theorem [23] is applied to nondimensionalize Eq. (1), thereby reducing the number of variables and simplifying the analysis into Eq. (2). The independent parameters, a^*, L^*, α, c^*, Re and P^* define the geometry, operating conditions, and fluid properties that influence the dependent parameters (Eqs. (3)–(8)). W_r^*, W_a^*, F^* and Q^* are dimensionless parameters dependent on the system's operational characteristics, representing the radial load coefficient, axial load coefficient, friction coefficient, and flow coefficient, respectively (Eqs. (9)–(12)).

$$F^*, Q^*, W_r^*, W_a^* = f(a^*, L^*, \alpha, c^*, \mathrm{Re}, P^*) \tag{2}$$

$$a^* = \frac{a}{L} \tag{3}$$

$$L^* = \frac{L}{D} \tag{4}$$

$$\alpha \tag{5}$$

$$c^* = \frac{c}{D} \tag{6}$$

$$Re = \frac{\rho U c}{\mu} \tag{7}$$

$$P^* = \frac{\Delta P}{\frac{1}{2}\rho U^2} \tag{8}$$

$$F^* = \frac{F}{\frac{1}{2}\rho U^3 D L} \tag{9}$$

$$W_r^* = \frac{W_r}{\frac{1}{2}\rho U^2 \pi D \frac{L}{\cos(\alpha)}} \tag{10}$$

$$W_a^* = \frac{W_a}{\frac{1}{2}\rho U^2 \pi D \frac{L}{\cos(\alpha)}} \tag{11}$$

$$Q^* = \frac{Q}{U D^2} \tag{12}$$

3.3 Design of Experiments. These independent nondimensional parameters are systematically varied across three levels, as detailed in Table 3, to ensure a comprehensive exploration of the design space. Notably, a^*, L^*, and α align with the design parameters considered in the preliminary research, maintaining consistency in the analytical framework. The orifice diameter is fixed at 1 mm for all cases to eliminate the influence of orifice size on the results. The supply pressure varies depending on the case, with pressure differences of 5, 10, and 15 bar applied at the orifice inlets. For each case, the tangential speed at the maximum diameter of the shaft is maintained at a constant value of 252 m/s. All dimensional parameters, along with their ranges before nondimensionalization, are presented in Table 5.

Table 3 Levels of independent nondimensional groups

Level	a^*	L^*	α	c^*	Re	P^*
1	0.1	0.5	10	0.0033	10,363	0.02837
2	0.25	0.75	15	0.0042	20,727	0.05674
3	0.4	1	20	0.006	31,090	0.08511

In a full factorial design, obtaining information about interactions would necessitate conducting 729 experiments. To minimize this extensive experimentation, Taguchi's L27 orthogonal array [24] is employed, which accommodates six factors, each at three levels, reducing the number of required experiments to just 27, as shown in Table 2. However, the relationship between the dependent and independent parameters is a priori unknown. To uncover the relevant trends, a parametric perturbation analysis is conducted, one dimensionless parameter is varied at a time while keeping the others constant at level 2, as outlined in Table 7. Following the parametric analysis, CFD data obtained by Taguchi's L27 orthogonal array are processed using symbolic regression techniques implemented in PYTHON with the open-source PySR library [25], enabling an accurate representation of the relationships between parameters and performance metrics. As symbolic regression finds mathematical expressions describing relationships between variables without assuming a predefined form, the independent and dependent variables are provided as input, and the search space for potential models is defined with population sizes selected between 40 and 100 to balance model diversity and computational cost. The algorithm utilized binary operators such as +, −, *, /, and ^ to explore different mathematical expressions. The models are then validated using test data and compared based on their Root Mean Square Error (RMSE), Mean Absolute Error (MAE), and coefficient of determination values.

4 Results

4.1 Representative Bearing Performance and Parametric Perturbation Analysis. In the preliminary research, the representative geometry described in the Methodology section is analyzed to gain a general understanding, providing insights into the fluid dynamics of the high-speed hybrid conical bearings. Figure 9 illustrates the results of the CFD analysis, presenting the distribution of pressure, skin friction, and vapor volume fraction across the lubricated surface. Bearing eccentricity induces pressure asymmetry between pockets, resulting in localized pressure peaks of up to 1.9 MPa. The interaction with the rotor's high tangential velocity induces vorticity and circulation (Fig. 9(*a*)), leading to regions of high shear stress and increased skin friction beneath the recesses.

Table 4 The comparison of R^2, RMSE and MAE values between the models

	R^2	RMSE	MAE
Q^* Train	0.99	2.9e−05	2.2e−05
Q^* Test	0.96	5.2e−05	4.6e−05
F^* Train	0.99	1.1e−04	8.6e−05
F^* Test	0.94	1.8e−04	1.4e−04
W_r^* Train	0.99	3.3e−04	2.8e−04
W_r^* Test	0.93	7.1e−04	5.7e−04
W_a^* Train	0.97	2.7e−04	2.1e−04
W_a^* Test	0.91	2.5e−04	2.3e−04

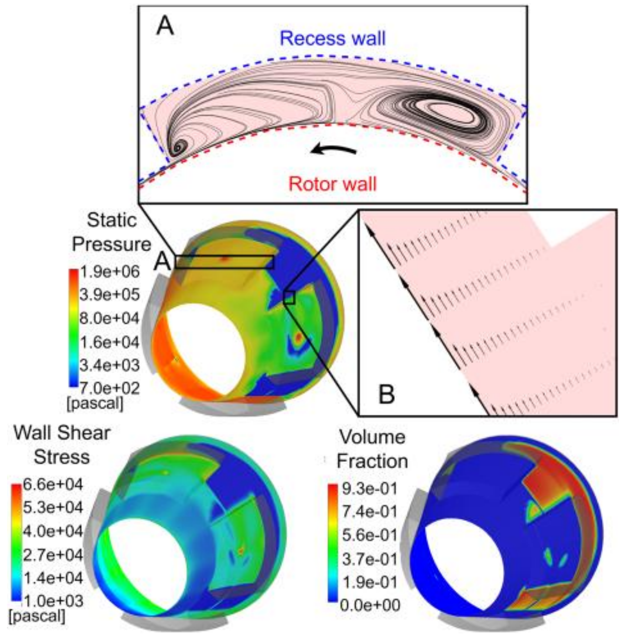

Fig. 9 The distributions of pressure, skin friction, and volume fraction on the rotor surface

In the landing zones, tangential acceleration from the recesses reduces flow non-uniformity, mitigating excessive skin friction on the shaft surface (Fig. 9(*b*)). The acceleration also induces localized pressure drops, and when the pressure falls below the lubricant's vaporization threshold, cavitation occurs, leading to the formation of vapor regions, particularly in high-radius areas. As a result, skin friction is significantly reduced within these cavitation zones.

In the following, a parametric perturbation analysis is conducted, where one dimensionless parameter is varied at a time, while the others are held constant at level 2 defined in Table 3. The quantitative relationships of the investigated free variables with respect to the nondimensional flowrate, friction, radial load, and axial load are presented in Figs. 10–13, respectively. It is found that the relationship between a^* and Q^* is linear, while the others follow a power-law trend. These findings provide a more precise understanding of how small changes in the bearing parameters can significantly affect performance. By revealing the relationships between various parameters and performance metrics, the analysis lays the groundwork for improving bearing designs. Furthermore, the parametric analysis was essential in creating the meta-models used for predicting bearing performance. The relationships identified through this analysis were used to construct the meta-models, which were then fitted using least squares to capture the power-law trends observed. This method ensures that the meta-models can predict bearing performance with greater accuracy across a range of operational conditions. In addition, the parametric analysis also provided insights into the pressure, shear stress, and cavitation contours, further informing the bearing design process.

For variations in the axial extent of the landings in the recessed regions (Fig. 14) illustrates that as a^* increases, the flow coefficient decreases (almost linearly, Fig. 10), primarily due to the reduced fluid entry and increased flow resistance. However, this augments the extent of the cavitation regions. On the other hand, the friction coefficient exhibits a sharp decline following a concave downward trend (Fig. 11), as a smaller recess area results in lower shear stress on the bearing surfaces. Additionally, both the radial and axial load coefficients decrease in a concave downward manner (Figs. 12 and 13, respectively) with a growth of a^*, which can be attributed to the diminished hydrostatic pressure distribution, thereby limiting the bearing's load-carrying capacity.

When nondimensional length (L^*) increases (Fig. 15), the flow coefficient exhibits a greater than linear growth (Fig. 10) due to enhanced suction, driven by the increasing radius of the rotating conical shaft. The friction coefficient also decreases with power-law decay trend (Fig. 11), as the extended bearing promotes a wider cavitation zone, reducing shear stress. Meanwhile, the radial load coefficient increases at a decreasing rate (Fig. 12) as the greater distance to the discharge locations enhances tangential pressure asymmetry. However, the axial load coefficient exhibits minimal variation between the two extremes, exhibiting an inverted parabolic behavior (Fig. 13). The influence of increasing cone angle α is illustrated in Fig. 16. While other parameters are constant, the flow coefficient increases due to the reduced bearing area, which lowers flow resistance, as well as enhanced suction, driven by the increasing radius of the rotating conical shaft. The friction coefficient decreases despite a similar cavitated volume fraction, as the effective area reduces for a given maximum diameter. As expected, the radial

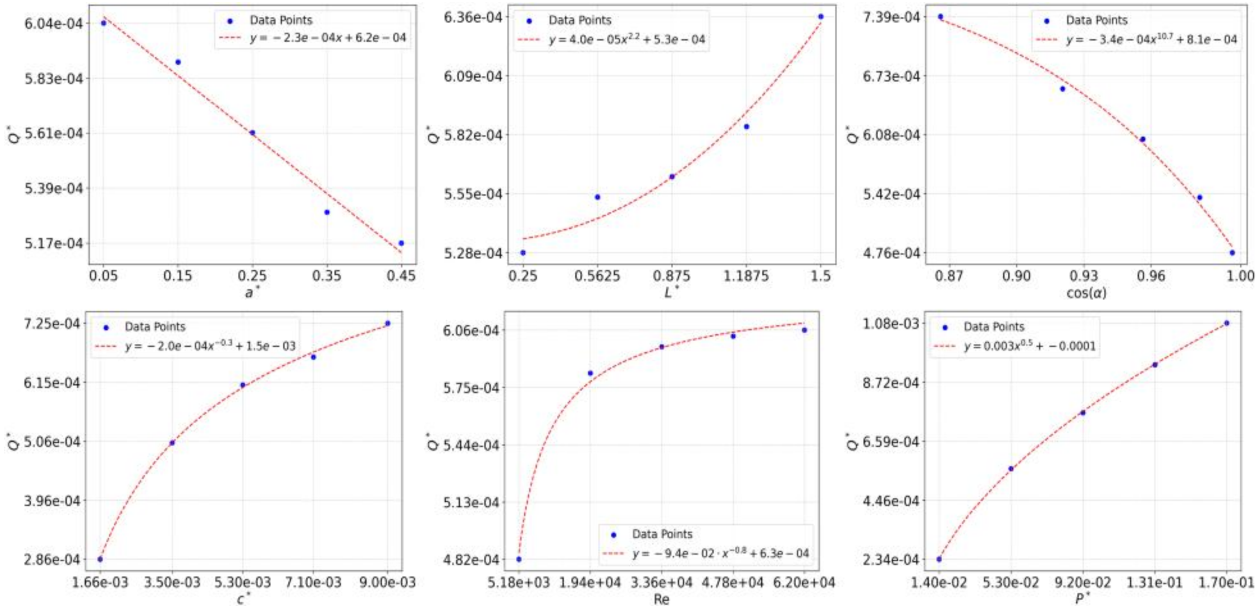

Fig. 10 Dependency of nondimensional flow coefficient Q^* to a^*, L^*, α, c^*, Re, and P^*

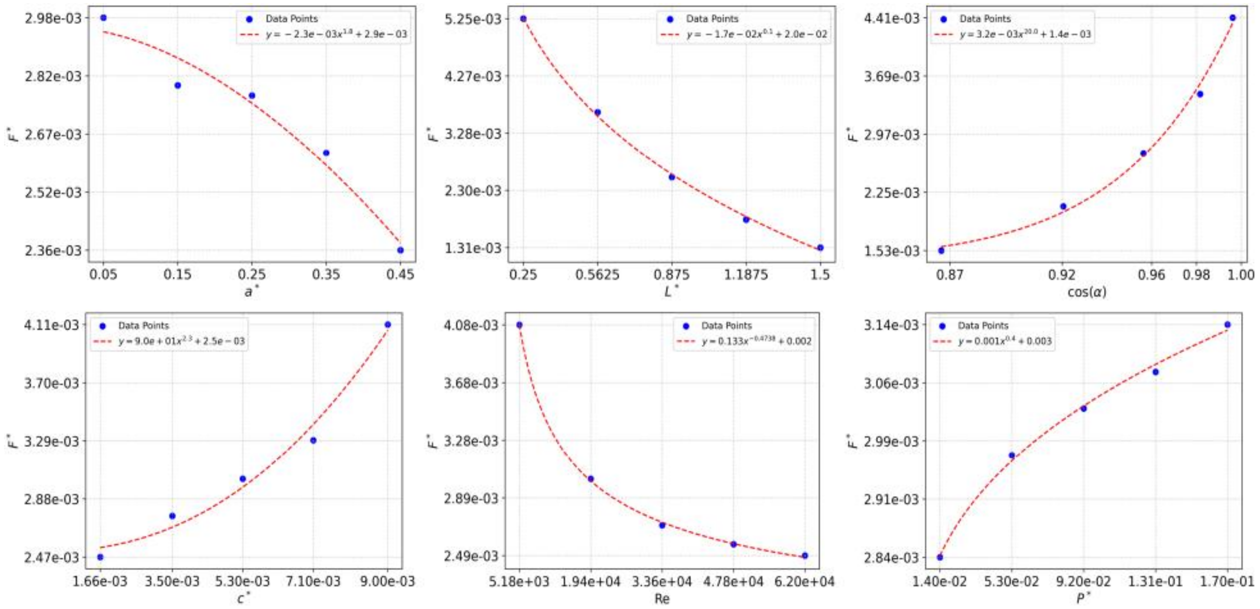

Fig. 11 Dependency of nondimensional friction coefficient F^* to a^*, L^*, α, c^*, Re, and P^*

load coefficient continuously decreases as the angle increases, resulting in geometric increase in axial load coefficient (Figs. 10–13 illustrate the power-law variation of these parameters as a function of the sine and cosine of α). The effect of nondimensional clearance (c^*) is presented in Fig. 17. As c^* increases, the clearance enlarges, permitting a higher fluid flow for the same supply pressure, which leads to an increase in the flow coefficient (Fig. 10). The friction coefficient also increases following an accelerating power-law trend (Fig. 11), primarily due to the significantly higher flowrate and enhanced cavitation. However, both the radial and axial load coefficients decrease with power-law decay (Figs. 12 and 13), as the larger clearance reduces hydrostatic pressure buildup, weakening the bearing's ability to carry loads. Another important parameter influencing the performance of hydrostatic conical bearings is the Reynolds number (Fig. 18). Figures 10 and 11 reflect that as the Re increases, the flow coefficient exhibits a power-law increase, while the friction coefficient decreases due to reduced viscous effects. Both the radial and axial load coefficients tend to diminish following a power-law decay (Figs. 12 and 13) as larger inertial effects reduce hydrostatic pressure buildup, which relies on friction (to block the flow in the narrower gap), thereby weakening the bearing's load-carrying capacity. Finally, the effect of the nondimensional supply pressure is demonstrated in Fig. 19. As P^* increases, the flow coefficient increases due to increased kinetic energy of the fluid for a fixed effective area. Expectedly, the friction coefficient also augments as higher flow velocities generate greater shear stress within the fluid film. Ultimately, both the radial and axial load coefficients rise with an increasing pressure coefficient, enhancing the bearing's hydrostatic capacity, which depends on the supply pressure, following a decaying power-law trend.

The primary objective of this study is to identify parametric trends and develop dimensionless performance correlations. As these trends remain qualitatively valid under isothermal conditions,

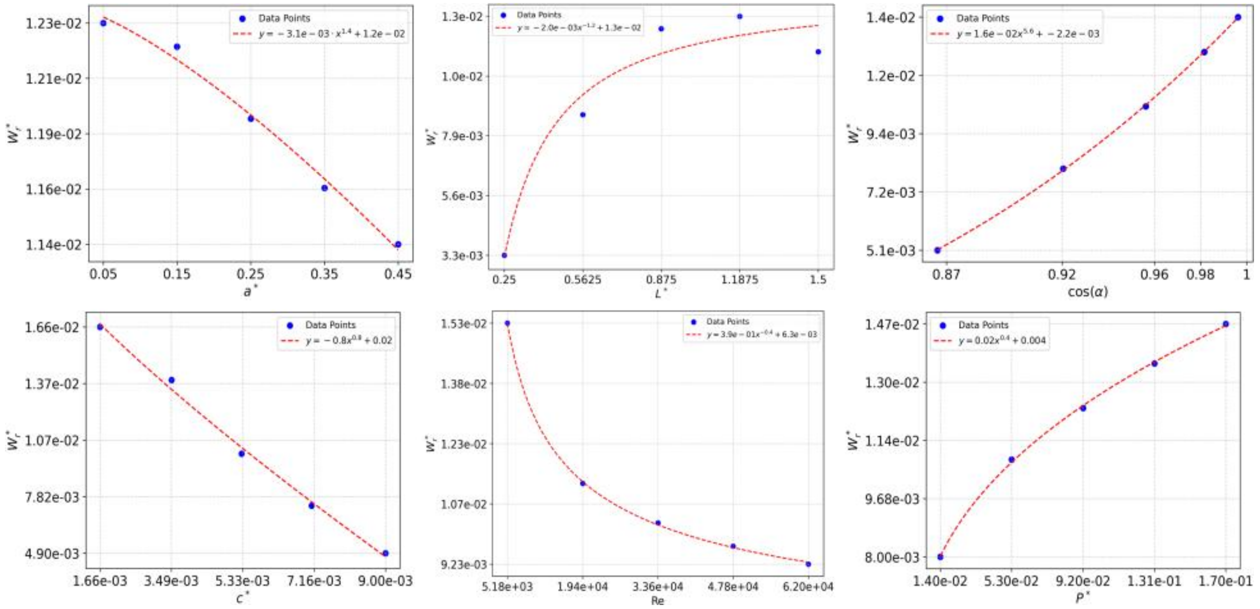

Fig. 12 Dependency of nondimensional radial load coefficient W_r^* to a^*, L^*, α, c^*, Re and P^*

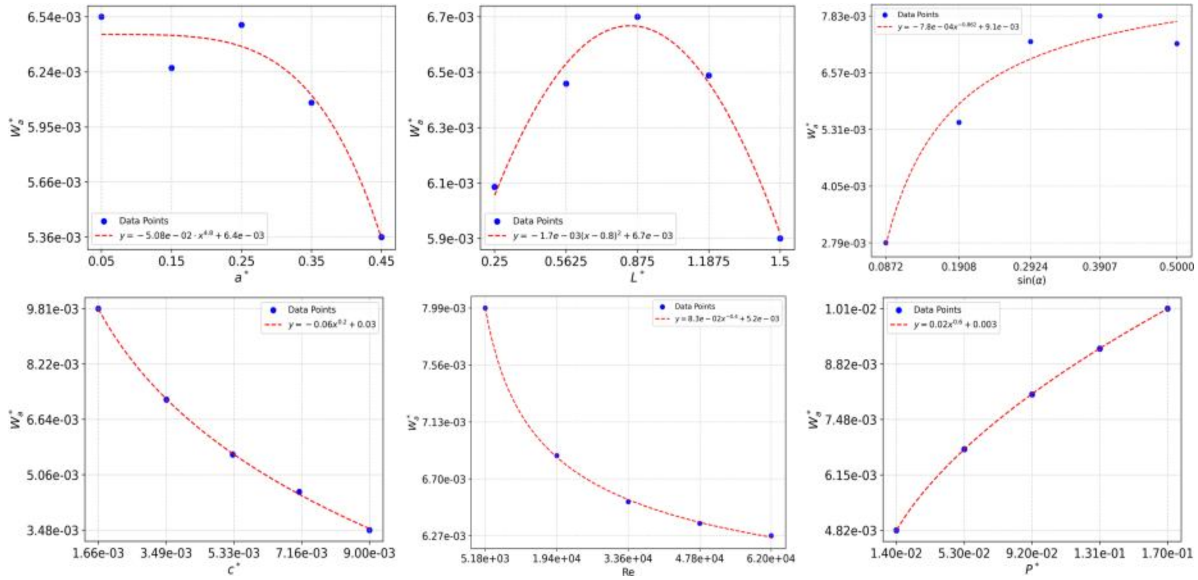

Fig. 13 Dependency of nondimensional axial load coefficient W_a^* to a^*, L*, α, c*, Re and P^*

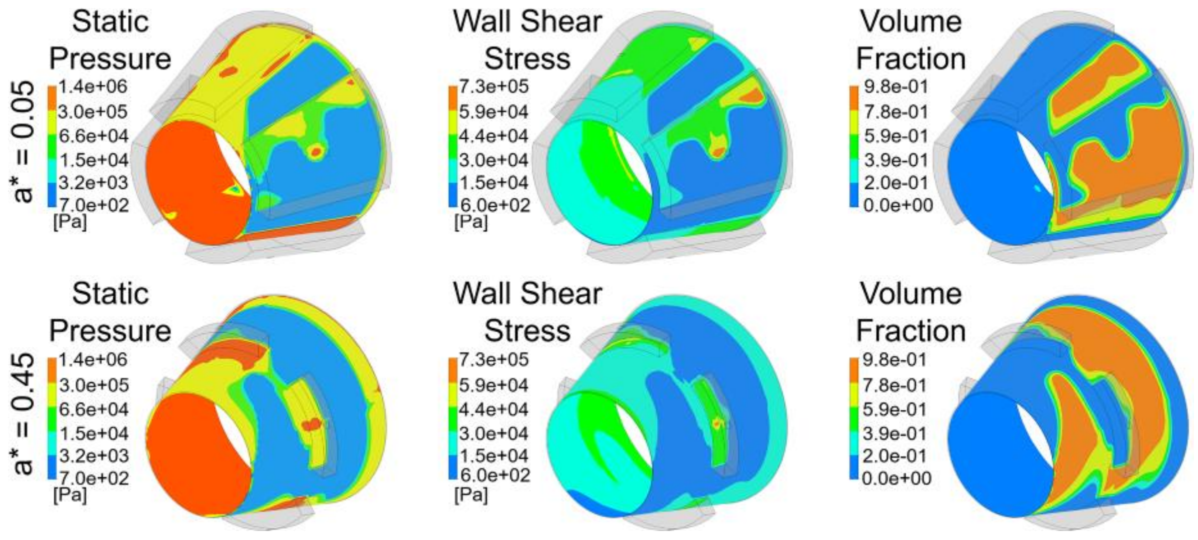

Fig. 14 For perturbed values of nondimensional axial extent of the landing in the recessed regions, $a^* = 0.05$ and 0.45, respectively, comparison of static pressure, wall shear stress, and volume fraction

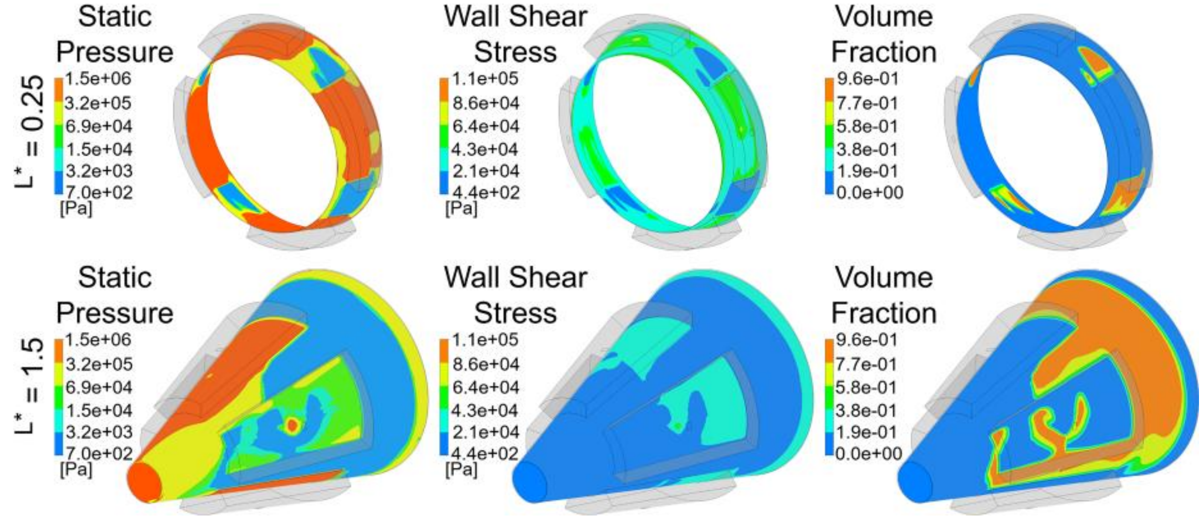

Fig. 15 For perturbed values of nondimensional length, $L^* = 0.15$ and 1.5 respectively, comparison of static pressure, wall shear stress, and volume fraction

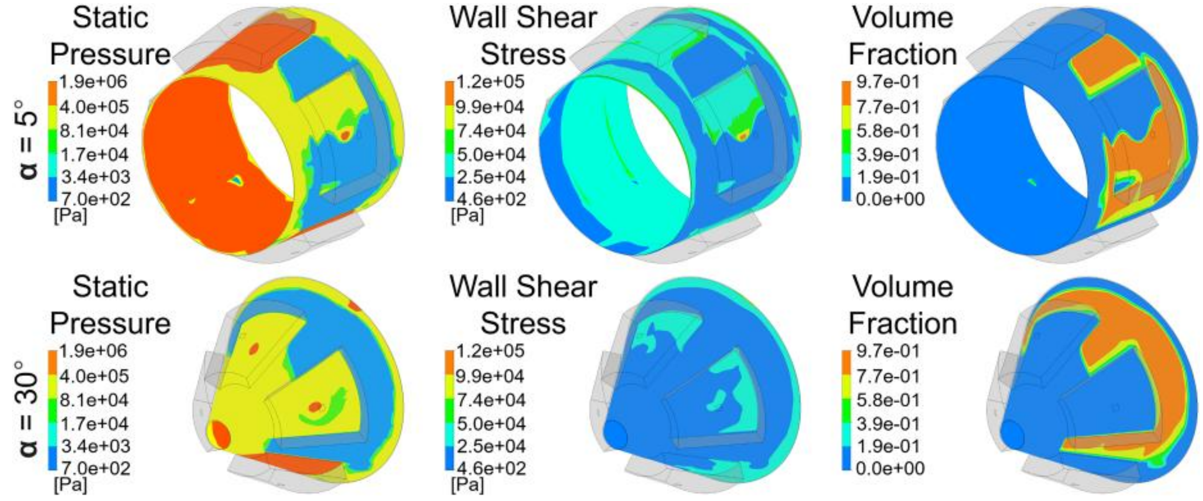

Fig. 16 For perturbed values of nondimensional cone angle, $\alpha = 5$ deg and 30 deg, respectively, comparison of static pressure, wall shear stress, and volume fraction

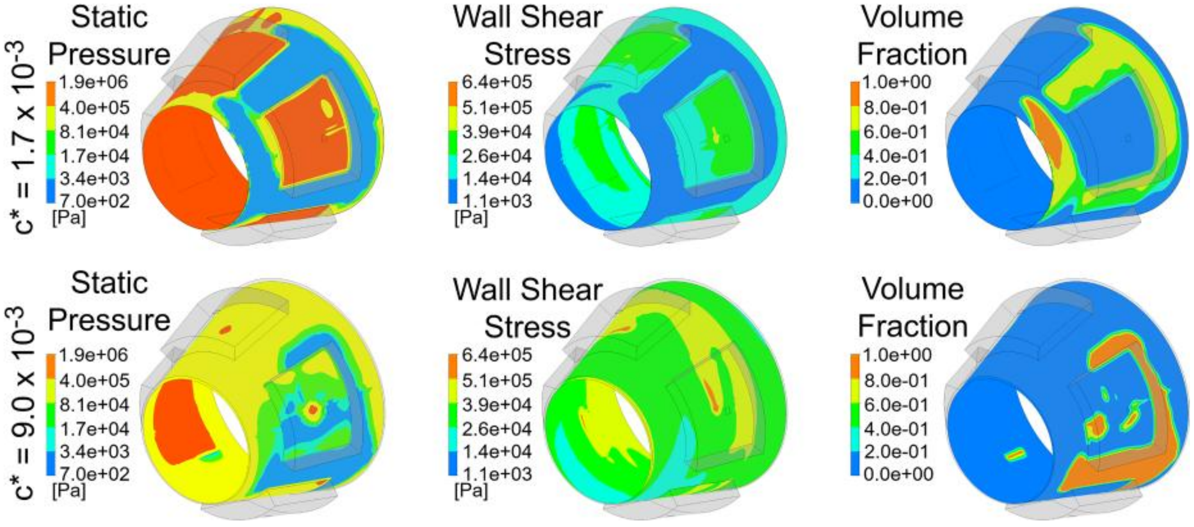

Fig. 17 For perturbed values of nondimensional clearance, $c^* = 1.7\text{E}{-3}$ and $9\text{E}{-3}$ respectively, comparison of static pressure, wall shear stress, and volume fraction

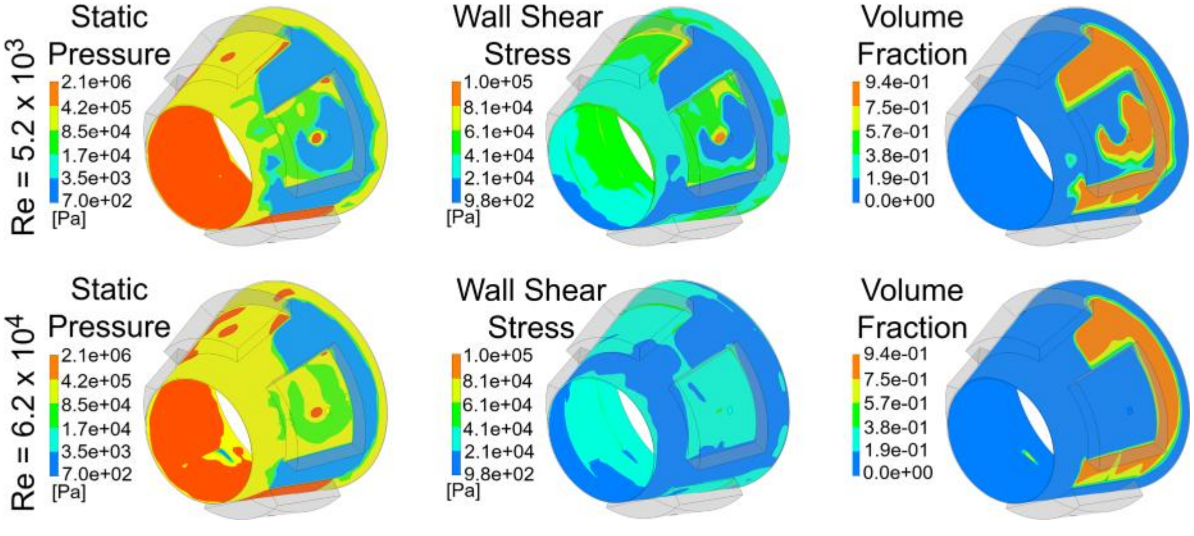

Fig. 18 For perturbed values of nondimensional Reynolds number, $\text{Re} = 5.2\text{E}+3$ and $6.2\text{E}+4$ respectively, comparison of static pressure, wall shear stress, and volume fraction

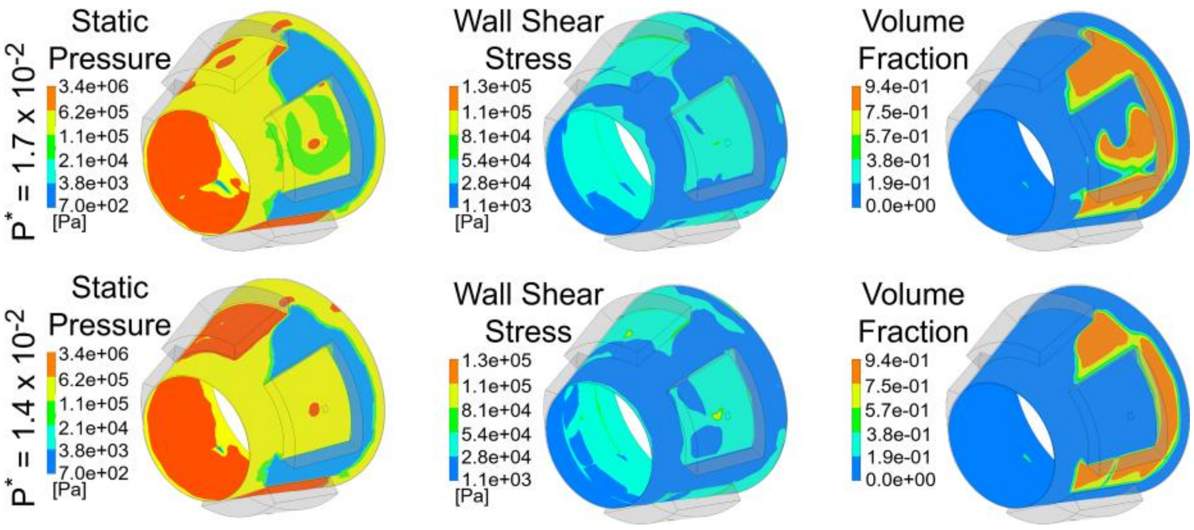

Fig. 19 For perturbed values of nondimensional supply pressure, $P^* = 1.7\text{E}{-2}$ and $1.4\text{E}{-2}$ respectively, comparison of static pressure, wall shear stress, and volume fraction

thermal effects were excluded in this preliminary modeling stage. Notably, the trends observed for the land-to-pocket ratio (a/L) and length-to-diameter ratio (L/D) align with those reported by Rowe [18], reinforcing the suitability of the isothermal assumption for capturing the dominant geometric influences on bearing behavior.

4.2 Correlation Characterizing Bearing Performance.

Parametric analysis helps uncover nonlinear trends and interactions between variables, providing valuable insights into the system's behavior. The relationships in this study predominantly follow power-law, exponential, or trigonometric functions. Building on these trends and utilizing the Taguchi data as a training set (Table 6), the symbolic regression analysis is conducted, yielding the following expressions for the flow, friction, radial load, and axial load coefficients as a function of the free variables:

$$Q^* = c^{*\cos\alpha}\left(\frac{a^*}{\cos\alpha} + 372.0653c^*\right) \times \left(P^*(\cos^2\alpha)^{\left(\frac{\text{Re}}{L^*}\right)^{P^*}} + 0.0231\right)^{\cos\alpha} \tag{13}$$

$$F^* = \frac{c^* + \left(0.0133 + \dfrac{0.010020283}{L^*}\right)\left(\cos^{10.6389^{a^*+L^*}}\alpha + P^*\right)}{\text{Re}^{0.2082}} \tag{14}$$

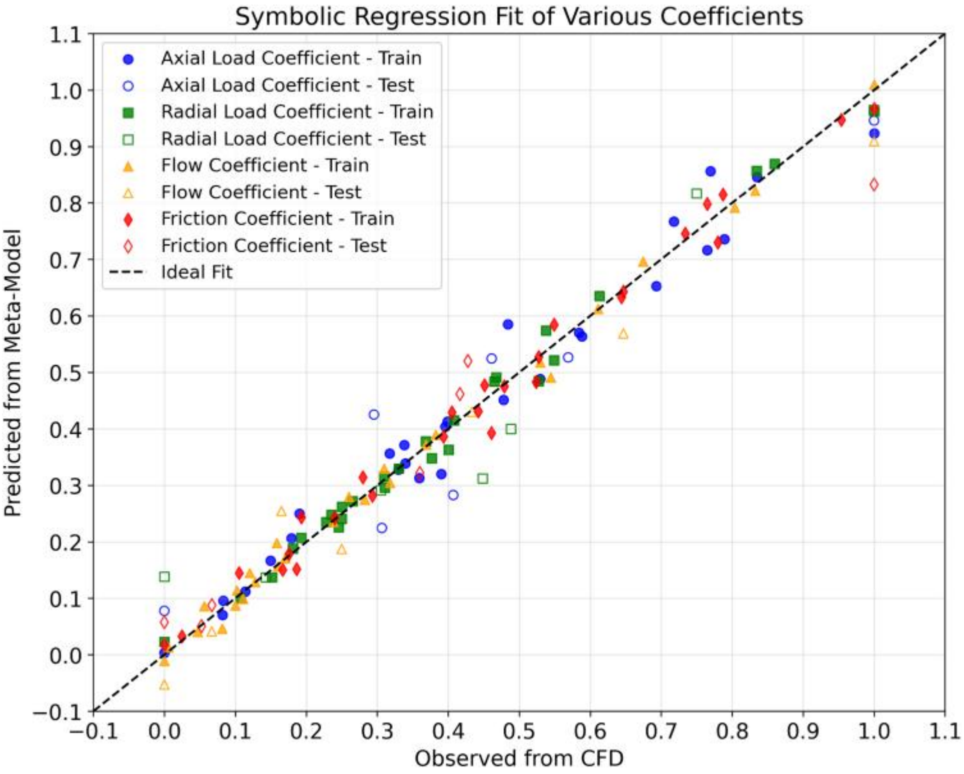

Fig. 20 The comparison between CFD-observed data (Tables 2 and 4) and meta-model predictions (Eqs. (13)–(16))

$$W_r^* = L^* \left(\left(\cos^{L^{*\left(\frac{a^*}{P^*+0.0757}\right)^{1.7887}}} \alpha + P^* \right) (-c^{*\cos\alpha} + \mathrm{Re}^{-0.5206} + 0.8254) - 0.0705 \right) - 1.4175 \times 10^{-3} \tag{15}$$

$$W_a^* = (\sin\alpha + 0.1337) \left(c^* + \left(\frac{P^*}{\left(\frac{\mathrm{Re}}{L^*}\right)^{0.2849}} + \frac{c^{*2}}{a^*(a^* - 0.4374)} \right) 1.8208 + 0.0076 \right) \tag{16}$$

To evaluate the predictive accuracy of the models, Fig. 20 presents a comparison between the CFD results and the corresponding model predictions. The CFD data comprise both the Taguchi training dataset from Table 6 and the test dataset from Table 8. Empty markers denote test data, while filled markers indicate training data. The dashed line indicates the locus of points where model predictions exactly match the experimental data, representing ideal predictive accuracy. Four models (Eqs. (13)–(16)) are tested in the figure: the Axial and Radial Load Coefficients, the Friction Power Loss Coefficient, and the Flow Coefficient. In order to ensure a consistent basis for comparison, both the predicted and observed coefficients were normalized using the data range of the observed values:

$$x_{norm} = \frac{x_{obs} - x_{obs,min}}{x_{obs,max} - x_{obs,min}}$$

$$y_{norm} = \frac{y_{pred} - x_{obs,min}}{x_{obs,max} - x_{obs,min}}$$

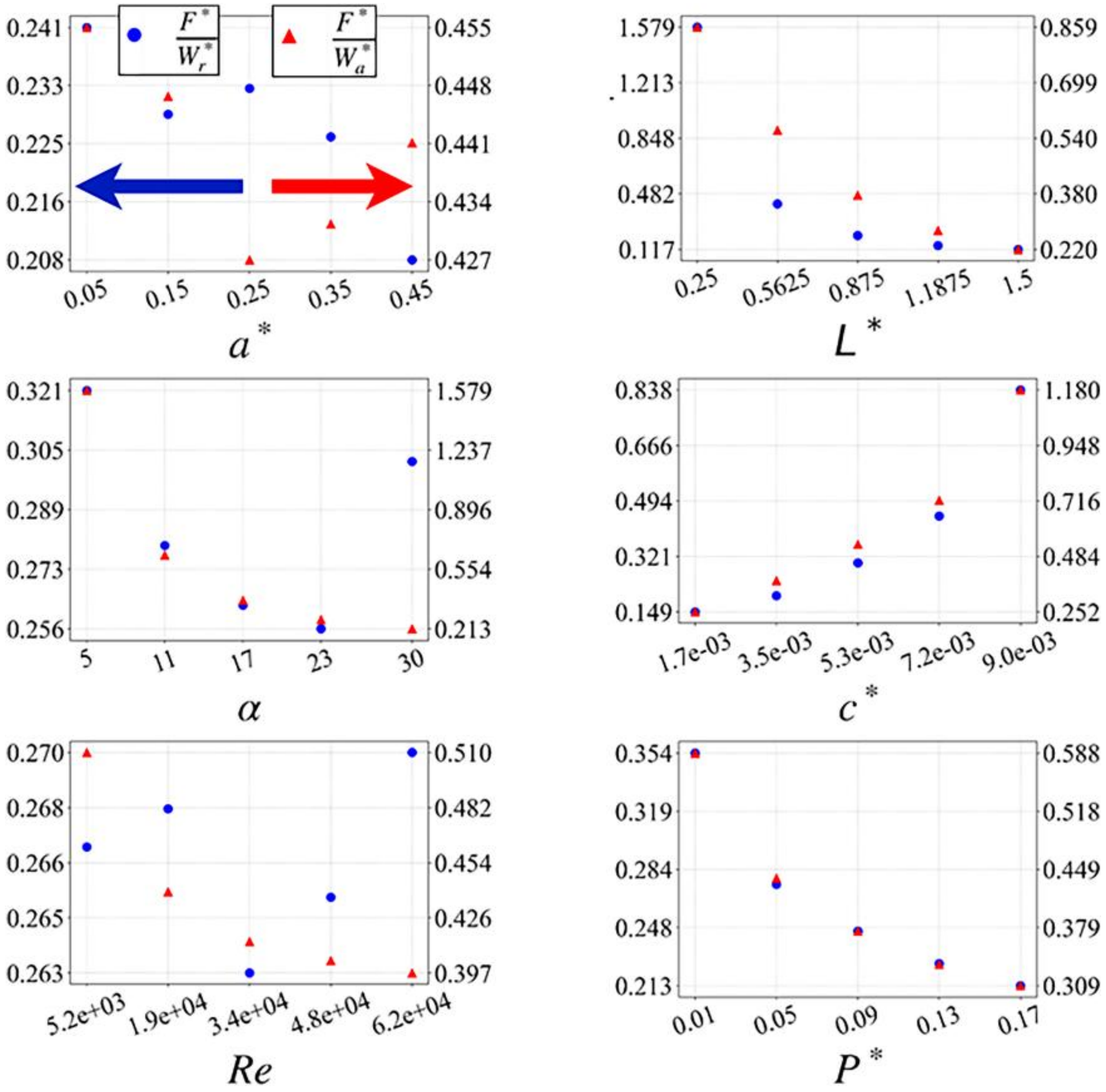

Fig. 21 Variation of the dimensionless parameters F^*/W_r^* and F^*/W_a^* with respect to independent variables

Here, x_{norm} and y_{norm} denote the normalized CFD-observed and model-predicted coefficients, respectively, while x_{obs} and y_{pred} represent their non-normalized counterparts. The minimum and maximum values of the CFD-observed coefficients are denoted by $x_{obs,min}$ and $x_{obs,max}$, respectively.

The R^2, RMSE, and MAE values for both the training (Table 6) and test (Table 8) datasets are summarized in Table 4. The R^2 values exceed 0.9 for both datasets, indicating (together with Fig. 20) a strong correlation between the model predictions and the CFD-observed values. Consistently low RMSE and MAE values across both datasets further substantiate the model's predictive accuracy. Particularly noteworthy is the model's performance on the independent test dataset, which was excluded from the training phase. Its ability to reliably predict previously unseen data highlights the model's robustness, generalization capability, and practical applicability. Collectively, these results demonstrate that the model not only provides a strong fit to the training data but also maintains high predictive fidelity when applied to new cases, thereby confirming its validity for broader implementation.

In addition to the developed model that characterizes the design parameters of a high-speed hybrid bearing with large clearance, compliant with additive manufacturing constraints, supplementary design charts have also been constructed to offer practical guidance for designers. These charts complement the seminal work of Rowe, whose original charts were confined to bearings with smaller clearances and cavitation-free operating conditions. Toward this goal, Fig. 21 illustrates the relationship between the dimensionless parameters and bearing performance. The graph displays F^*/W_r^* on the primary y-axis and F^*/W_a^* on the secondary y-axis, representing the frictional power relative to the radial and axial load coefficients, respectively. Minimization of these two parameters is sought to identify the optimal operating point. Six separate plots are presented, each corresponding to a nondimensional parameter on the x-axis: a^*, L^*, α, c^*, Re, and P^*. These parameters, which are the same as those used in the parametric analysis, are given in Table 7 of the Appendix. The analysis helps to understand their influence on bearing performance, particularly in terms of friction and load capacity.

The results indicate that, for optimal performance, the nondimensional parameter a* should exceed 0.25, which is consistent with Rowe's design recommendations for recessed journal bearings [18]. Furthermore, the analysis identifies an optimal semi-cone angle (α) of approximately 23 deg. A significant outcome of the study is that minimizing the bearing clearance (c^*) is crucial for reducing frictional losses while enhancing load-carrying capacity. Additionally, while maximizing the pressure coefficient is desirable, the incremental benefit diminishes beyond a value of approximately 0.17. Similarly, the axial length-to-diameter ratio (L^*) should exceed unity to improve overall performance. Another noteworthy finding is the identification of an optimal Reynolds number that simultaneously supports favorable conditions for both radial and axial load capacities while minimizing frictional power losses.

In summary, these charts serve as guidelines for optimizing bearing geometry by helping designers balance friction power loss with radial and axial load capacities through appropriate parameter selection.

5 Conclusions

This study provided a comprehensive investigation of recessed conical hybrid bearings operating at turbine-level peripheral speeds under large-clearance, high-Reynolds-number conditions representative of additive manufacturing constraints, taking advantage of recent AM capabilities to enable integrated, optimized bearing–rotor architectures. By combining a Design-of-Experiments methodology with high-fidelity Navier–Stokes simulations, the effects of geometry, clearance size, supply pressure, recess configuration, semi-cone angle, rotational speed, and fluid properties on load capacity, frictional losses, and flowrates were quantified. The results revealed that turbine-speed operation induces complex three-dimensional flow interactions and cavitation phenomena that significantly limit the predictive accuracy of classical hydrodynamic models. A key outcome of this research is the derivation of compact correlations between critical nondimensional parameters using symbolic regression, achieving predictive accuracies within 15% even in the most challenging regimes, thus providing practical tools for the rapid design and optimization of high-speed conical hybrid bearings. Complementary graphical design aids further enhance the applicability of the findings to real-world bearing-integrated turbomachinery development. In practical terms, the study identified several tendencies that can serve as rules of thumb for designers: a recess axial extent below half of the bearing length is associated with lower power loss while preserving support; a semi-cone angle near 23 deg offers a balanced compromise between load capacity and friction; smaller radial clearance within additive manufacturing tolerances promotes reduced losses together with higher load-carrying capacity; overall performance improves when axial length is at least equal to, and preferably greater than, the diameter; while increasing the pressure coefficient is beneficial, the marginal gains diminish beyond approximately 0.17.

Funding Data

- The NATO Science for Peace and Security Programme under grant G5939-Additively Printed Engine (APE).
- The İzmir Katip Çelebi University Scientific Research Projects Coordination Office under Project No. 2023-TYL-FEBE-0018.

Conflict of Interest

There are no conflicts of interest.

Data Availability Statement

The datasets generated and supporting the findings of this article are obtainable from the corresponding author upon reasonable request.

Nomenclature

a = axial bearing land width, m
c = clearance, m
D = maximum diameter of the bearing, m
F = friction loss, W
L = length of the bearing, m
Q = volume flowrate, m^3/s
U = tangential speed at the maximum radius, m/s
a^* = axial land ratio
c^* = clearance-to-diameter ratio
F^* = friction coefficient
L^* = length-to-diameter ratio
P^* = pressure coefficient
Q^* = flow coefficient
S_h = performance parameter
W_a = axial load capacity, N
W_r = radial load capacity, N
W_a^* = axial load coefficient
W_r^* = radial load coefficient
Re = Reynolds number
ΔP = supply total-to-exit static pressure difference, Pa
α = semi-cone angle, deg
μ = dynamic viscosity, Pa · s
ρ = density of the lubricant, kg/m^3

Appendix: Data Tables

Table 5 Dimensional parameter ranges (pre-nondimensionalization)

	a (m)	L (m)	c (m)	α	D (m)	U (m/s)	ΔP (Pa)	μ (Pa.s)	ρ (kg/m^3)
L1	0.0045	0.045	0.0003	10	0.09	212.58	500,000	0.0048	780
L2	0.0045	0.045	0.0003	10	0.09	212.58	1,000,000	0.0024	780
L3	0.0045	0.045	0.0003	10	0.09	212.58	1,500,000	0.0016	780
L4	0.00525	0.0525	0.0003	15	0.07	212.58	500,000	0.0048	780
L5	0.00525	0.0525	0.0003	15	0.07	212.58	1,000,000	0.0024	780
L6	0.00525	0.0525	0.0003	15	0.07	212.58	1,500,000	0.0016	780
L7	0.005	0.05	0.0003	20	0.05	212.58	500,000	0.0048	780
L8	0.005	0.05	0.0003	20	0.05	212.58	1,000,000	0.0024	780
L9	0.005	0.05	0.0003	20	0.05	212.58	1,500,000	0.0016	780
L10	0.00625	0.025	0.0003	15	0.05	212.58	1,000,000	0.0048	780
L11	0.00625	0.025	0.0003	15	0.05	212.58	1,500,000	0.0024	780
L12	0.00625	0.025	0.0003	15	0.05	212.58	500,000	0.0016	780
L13	0.016875	0.0675	0.0003	20	0.09	212.58	1,000,000	0.0048	780
L14	0.016875	0.0675	0.0003	20	0.09	212.58	1,500,000	0.0024	780
L15	0.016875	0.0675	0.0003	20	0.09	212.58	500,000	0.0016	780
L16	0.0175	0.07	0.0003	10	0.07	212.58	1,000,000	0.0048	780
L17	0.0175	0.07	0.0003	10	0.07	212.58	1,500,000	0.0024	780
L18	0.0175	0.07	0.0003	10	0.07	212.58	500,000	0.0016	780
L19	0.014	0.035	0.0003	20	0.07	212.58	1,500,000	0.0048	780
L20	0.014	0.035	0.0003	20	0.07	212.58	500,000	0.0024	780
L21	0.014	0.035	0.0003	20	0.07	212.58	1,000,000	0.0016	780
L22	0.015	0.0375	0.0003	10	0.05	212.58	1,500,000	0.0048	780
L23	0.015	0.0375	0.0003	10	0.05	212.58	500,000	0.0024	780
L24	0.015	0.0375	0.0003	10	0.05	212.58	1,000,000	0.0016	780
L25	0.036	0.09	0.0003	15	0.09	212.58	1,500,000	0.0048	780
L26	0.036	0.09	0.0003	15	0.09	212.58	500,000	0.0024	780
L27	0.036	0.09	0.0003	15	0.09	212.58	1,000,000	0.0016	780
Test1	0.009778	0.05146	0.0003	14	0.079177	212.58	761,541.7	0.002409	780
Test2	0.003785	0.03154	0.0003	12	0.05735	212.58	1,399,890	0.001747	780
Test3	0.009887	0.04494	0.0003	17	0.052873	212.58	578,426.2	0.001827	780
Test4	0.022391	0.05892	0.0003	16	0.084175	212.58	813,709.3	0.001627	780
Test5	0.011944	0.03981	0.0003	18	0.066357	212.58	1,095,168	0.002868	780
Test6	0.023077	0.06787	0.0003	13	0.075415	212.58	1,274,406	0.002173	780
Test7	0.016002	0.05715	0.0003	11	0.060156	212.58	673,949.4	0.003364	780
aL005	0.002625	0.0525	0.0003	15	0.07	212.58	1,000,000	0.0024	780
aL015	0.007875	0.0525	0.0003	15	0.07	212.58	1,000,000	0.0024	780
aL025	0.013125	0.0525	0.0003	15	0.07	212.58	1,000,000	0.0024	780
aL035	0.018375	0.0525	0.0003	15	0.07	212.58	1,000,000	0.0024	780
aL045	0.023625	0.0525	0.0003	15	0.07	212.58	1,000,000	0.0024	780
LD025	0.004375	0.0175	0.0003	15	0.07	212.58	1,000,000	0.0024	780
LD05625	0.009844	0.039375	0.0003	15	0.07	212.58	1,000,000	0.0024	780
LD0875	0.015313	0.06125	0.0003	15	0.07	212.58	1,000,000	0.0024	780
LD11875	0.020781	0.083125	0.0003	15	0.07	212.58	1,000,000	0.0024	780
LD15	0.02625	0.105	0.0003	15	0.07	212.58	1,000,000	0.0024	780
ALPHA5	0.013125	0.0525	0.0003	5	0.07	212.58	1,000,000	0.0024	780
ALPHA11	0.013125	0.0525	0.0003	11	0.07	212.58	1,000,000	0.0024	780
ALPHA17	0.013125	0.0525	0.0003	17	0.07	212.58	1,000,000	0.0024	780
ALPHA23	0.013125	0.0525	0.0003	23	0.07	212.58	1,000,000	0.0024	780
ALPHA30	0.013125	0.0525	0.0003	30	0.07	212.58	1,000,000	0.0024	780
cD00143	0.013125	0.0525	0.000117	15	0.07	212.58	1,000,000	0.000933	780
cD00191	0.013125	0.0525	0.000245	15	0.07	212.58	1,000,000	0.00196	780
cD00238	0.013125	0.0525	0.000373	15	0.07	212.58	1,000,000	0.002987	780
cD00333	0.013125	0.0525	0.000502	15	0.07	212.58	1,000,000	0.004013	780
cD00381	0.013125	0.0525	0.00063	15	0.07	212.58	1,000,000	0.00504	780
Re1	0.013125	0.0525	0.0003	15	0.07	212.58	1,000,000	0.009601	780
Re2	0.013125	0.0525	0.0003	15	0.07	212.58	1,000,000	0.002566	780
Re3	0.013125	0.0525	0.0003	15	0.07	212.58	1,000,000	0.001481	780
Re4	0.013125	0.0525	0.0003	15	0.07	212.58	1,000,000	0.001041	780
Re5	0.013125	0.0525	0.0003	15	0.07	212.58	1,000,000	0.000802	780
Pr1	0.013125	0.0525	0.0003	15	0.07	212.58	246,738.8	0.0024	780
Pr2	0.013125	0.0525	0.0003	15	0.07	212.58	934,082.6	0.0024	780
Pr3	0.013125	0.0525	0.0003	15	0.07	212.58	1,621,426	0.0024	780
Pr4	0.013125	0.0525	0.0003	15	0.07	212.58	2,308,770	0.0024	780
Pr5	0.013125	0.0525	0.0003	15	0.07	212.58	2,996,114	0.0024	780

Table 6 Taguchi's L27 orthogonal array

a^*	L^*	α	c^*	Re	P^*
0.1	0.5	10	0.0033	10,363	0.02837
0.1	0.5	10	0.0033	20,727	0.05674
0.1	0.5	10	0.0033	31,090	0.08511
0.1	0.75	15	0.0042	10,363	0.02837
0.1	0.75	15	0.0042	20,727	0.05674
0.1	0.75	15	0.0042	31,090	0.08511
0.1	1	20	0.006	10,363	0.02837
0.1	1	20	0.006	20,727	0.05674
0.1	1	20	0.006	31,090	0.08511
0.25	0.5	15	0.006	10,363	0.05674
0.25	0.5	15	0.006	20,727	0.08511
0.25	0.5	15	0.006	31,090	0.02837
0.25	0.75	20	0.0033	10,363	0.05674
0.25	0.75	20	0.0033	20,727	0.08511
0.25	0.75	20	0.0033	31,090	0.02837
0.25	1	10	0.0042	10,363	0.05674
0.25	1	10	0.0042	20,727	0.08511
0.25	1	10	0.0042	31,090	0.02837
0.4	0.5	20	0.0042	10,363	0.08511
0.4	0.5	20	0.0042	20,727	0.02837
0.4	0.5	20	0.0042	31,090	0.05674
0.4	0.75	10	0.006	10,363	0.08511
0.4	0.75	10	0.006	20,727	0.02837
0.4	0.75	10	0.006	31,090	0.05674
0.4	1	15	0.0033	10,363	0.08511
0.4	1	15	0.0033	20,727	0.02837
0.4	1	15	0.0033	31,090	0.05674

Table 7 Additional DoE campaign in which one dimensionless parameter was varied at a time while keeping the others constant at level 2

a^*	L^*	α	c^*	Re	P^*
0.05	0.75	15	0.0042	20,726	0.056
0.15	0.75	15	0.0042	20,726	0.056
0.25	0.75	15	0.0042	20,726	0.056
0.35	0.75	15	0.0042	20,726	0.056
0.45	0.75	15	0.0042	20,726	0.056
0.25	0.25	15	0.0042	20,726	0.056
0.25	0.5625	15	0.0042	20,726	0.056
0.25	0.875	15	0.0042	20,726	0.056
0.25	1.1875	15	0.0042	20,726	0.056
0.25	1.5	15	0.0042	20,726	0.056
0.25	0.75	5	0.0042	20,726	0.056
0.25	0.75	11	0.0042	20,726	0.056
0.25	0.75	17	0.0042	20,726	0.056
0.25	0.75	23	0.0042	20,726	0.056
0.25	0.75	30	0.0042	20,726	0.056
0.25	0.75	15	0.0016	20,726	0.056
0.25	0.75	15	0.0035	20,726	0.056
0.25	0.75	15	0.0053	20,726	0.056
0.25	0.75	15	0.0071	20,726	0.056
0.25	0.75	15	0.009	20,726	0.056
0.25	0.75	15	0.0042	5181	0.056
0.25	0.75	15	0.0042	19,386	0.056
0.25	0.75	15	0.0042	33,591	0.056
0.25	0.75	15	0.0042	47,795	0.056
0.25	0.75	15	0.0042	62,000	0.056
0.25	0.75	15	0.0042	20,726	0.014
0.25	0.75	15	0.0042	20,726	0.053
0.25	0.75	15	0.0042	20,726	0.092
0.25	0.75	15	0.0042	20,726	0.131
0.25	0.75	15	0.0042	20,726	0.17

Table 8 Test data

a^*	L^*	α	c^*	Re	P^*
0.19	0.65	14	0.003789	20,645	0.04321
0.12	0.55	12	0.005231	28,478	0.07943
0.22	0.85	17	0.005674	27,234	0.03282
0.38	0.7	16	0.003564	30,567	0.04617
0.3	0.6	18	0.004521	17,342	0.06214
0.34	0.9	13	0.003978	22,894	0.07231
0.28	0.95	11	0.004987	14,789	0.03824

References

[1] Ciulli, E., Forte, P., Libraschi, M., Naldi, L., and Nuti, M., 2018, "Characterization of High-Power Turbomachinery Tilting Pad Journal Bearings: First Results Obtained on a Novel Test Bench," Lubricants, **6**(1), p. 4.

[2] Raimondi, A. A., and Boyd, J., 1958, "A Solution for the Finite Journal Bearing and Its Application to Analysis and Design: I," ASLE Trans., **1**(1), pp. 159–174.

[3] Raimondi, A. A., and Boyd, J., 1958, "A Solution for the Finite Journal Bearing and Its Application to Analysis and Design: II," ASLE Trans., **1**(1), pp. 175–193.

[4] Raimondi, A. A., and Boyd, J., 1958, "A Solution for the Finite Journal Bearing and Its Application to Analysis and Design: III," ASLE Trans., **1**(1), pp. 194–209.

[5] Rossopoulos, G. N., and Papadopoulos, C. I., 2022, "A Journal Bearing Performance Prediction Method Utilizing a Machine Learning Technique," Proc. Inst. Mech. Eng., Part J: J. Eng. Tribol., **236**(10), pp. 1993–2003.

[6] Milčić, D., Alsammarraie, A., Madić, M., Krstić, V., and Milčić, M., 2021, "Predictions of Friction Coefficient in Hydrodynamic Journal Bearing Using Artificial Neural Networks," Strojniški vestnik—J. Mech. Eng., **67**(9), pp. 411–420.

[7] O'Donoghue, J. P., Rowe, W. B., and Hooke, C. J., 1969, "Design of Hydrostatic Bearings Using an Operating Parameter," Wear, **14**(5), pp. 355–362.

[8] Cusano, C., and Conry, T. F., 1974, "Design of Multi-Recess Hydrostatic Journal Bearings for Minimum Total Power Loss," ASME J. Eng. Ind., **96**(1), pp. 226–232.

[9] Ghosh, M. K., and Majumdar, B. C., 1980, "Design of Multirecess Hydrostatic Oil Journal Bearings," Tribol. Int., **13**(2), pp. 73–78.

[10] Rowe, W. B., and Koshal, D., 1980, "A New Basis for the Optimization of Hybrid Journal Bearings," Wear, **64**(1), pp. 115–131.

[11] Kurtin, K. A., Childs, D., Andres, L. S., and Hale, K., 1993, "Experimental Versus Theoretical Characteristics of a High-Speed Hybrid (Combination Hydrostatic and Hydrodynamic) Bearing," ASME J. Tribol., **115**(1), pp. 160–168.

[12] Nypan, L. J., Hamrock, B. J., Scibbe, H. W., and Anderson, W. J., 1972, "Optimization of Conical Hydrostatic Bearing for Minimum Friction," J. Lubr. Technol., **94**(2), pp. 136–142.

[13] Sharma, S. C., Phalle, V. M., and Jain, S. C., 2011, "Performance Analysis of a Multirecess Capillary Compensated Conical Hydrostatic Journal Bearing," Tribol. Int., **44**(5), pp. 617–626.

[14] Gangrade, A. K., Phalle, V. M., and Mantha, S. S., 2019, "Performance Analysis of a Conical Hydrodynamic Journal Bearing," Iran. J. Sci. Technol., Trans. Mech. Eng., **43**(3), pp. 559–573.

[15] Rowe, W. B., 2021, "Conical Hydrostatic Journal Bearings for High Speeds," Proc. Inst. Mech. Eng., Part J: J. Eng. Tribol., **235**(4), pp. 808–819.

[16] Palman, M., Agapovichev, A., Abraham, Y., Erenburg, E., Yildirim, A., Acarer, S., Chatel, A., et al., 2026, "Design-for-Additive-Manufacturing Approach for Support-Free, Pre-Assembled Micro Gas Turbines," ASME J. Eng. Gas Turbines Power., **148**(1), p. 011025.

[17] Singh, U. P., Swaminathan, S., and Phanikumar, G., 2022, "Thermo-Mechanical Approach to Study the Residual Stress Evolution in Part-Scale Component During Laser Additive Manufacturing of Alloy 718," Mater. Des., **222**, p. 111048.

[18] Rowe, W. B., 2013, *Hydrostatic, Aerostatic and Hybrid Bearing Design*, Butterworth-Heinemann, Oxford, UK.

[19] Ho, Y. S., and Chen, N. N. S., 1979, "Performance Characteristics of a Capillary-Compensated Hydrostatic Journal Bearing," Wear, **52**(2), pp. 285–295.

[20] Ergin, C. C., Verstraete, T., and Saracoglu, B. H., 2024, "The Design and Optimization of Additively Manufactured Radial Compressor of a Miniature Gas Turbine Engine," ASME J. Fluids Eng., **146**(7), p. 071108.

[21] ANSYS, Inc., 2022, *ANSYS Fluent Theory Guide, Release 2022 R2*, ANSYS, Inc., Canonsburg, PA. Available at: https://www.ansys.com.

[22] Guo, Z., Hirano, T., and Kirk, R. G., 2005, "Application of CFD Analysis for Rotating Machinery—Part I: Hydrodynamic, Hydrostatic Bearings and Squeeze Film Damper," ASME J. Eng. Gas Turbines Power, **127**(2), pp. 445–451.

[23] Fox, R. W., McDonald, A. T., and Mitchell, J. W., 2020, *Fox and McDonald's Introduction to Fluid Mechanics*, 10th ed., John Wiley & Sons, Hoboken, NJ.

[24] Stapenhurst, T., and Bendell, A., 1990, "Taguchi Methods," J. Oper. Res. Soc., **41**(9), pp. 887–888.

[25] Cranmer, M., 2023, "Interpretable Machine Learning for Science With PySR and SymbolicRegression.jl," arXiv:2305.01582 [astro-ph.IM].